Optimal Design and Placement of Omni-Cameras in Binocular Vision Systems for Accurate 3D Data Measurement

Shen-En Shih, *Student Member*, *IEEE*, and Wen-Hsiang Tsai, *Senior Member, IEEE*

***Abstract*—A new problem of automatically designing an optimal stereo vision system using two omni-directional catadioptric cameras to yield the highest 3D data accuracy is studied. Factors of the system configuration considered in the design include camera pose, FOV, and mirror shape. To find the optimal vision system configuration, an analytic formula is derived to model the 3D measurement error, which takes into consideration the variations of pixel-quantization precisions and angular resolutions in images by conducting error propagation analysis in the data computation process. The formula is then used in an optimization framework to find the optimal system configurations for different shapes of system setup environments. For regular cases with rectangular cuboid-shaped 3D measurement and camera placement areas, two fast algorithms are proposed to solve the problem, one being bisection-based and relatively slower for deriving the optimal solution; and the other faster using analytic formulas for deriving a sub-optimal solution which is proved to be close to the optimal one in precision. Experimental results of simulations and real application cases show the feasibility of the proposed method.**

***Index Terms*—stereo vision system, omni-cameras, optimal system configuration, 3D data measurement accuracy.**

I. Introduction

Human-computer interaction is an important research area of modern technologies, attracting more and more attention in recent years. To become a successful product, many commercial applications are seeking better interfaces for man-machine interaction. Two examples are the Nintendo Wii and the Microsoft Kinect in the home entertainment industry.

One way to offer friendly interfacing is to provide the 3D data of the user's movement, making it possible to interact with the computer without wearing or holding any device, like the case of using the Microsoft Kinect. In the meantime, the provision of a wide field of view (FOV) by a vision system is also desired in order to offer faster and more comfortable interaction. One approach is to use two wide-FOV cameras (such as fisheye or catadioptric omni-cameras) to compose a stereo vision system for capturing the visual information in the application environment. The main goal of this study is to investigate methods for designing binocular vision systems that can be used to acquire accurate 3D data. The type of system considered is composed of two catadioptric omni-cameras as depicted in Fig. 1, with each omni-camera consisting of a hyperboloidal-shaped mirror and a perspective camera.

Related to this study, Eisert and Girod [1] reconstructed 3D objects from images acquired by uncalibrated cameras by simultaneously estimating the camera-motion parameters and refining the object shape. Wang and Wu [2] recovered the projective depth for perspective 3-D Euclidean reconstruction by perspective factorization [3]. Starck *et al*. [4] constructed a 3D production studio using multiple cameras and gave suggestions for camera deployment. When constructing stereo vision systems, it is well known that the precision of the calculated 3D data is strongly affected by the system configuration [4]-[19], including the placements, directions, mirror shapes of the used cameras. Thus, it is desired in this study is to derive the *optimal configuration* of a stereo vision system to yield the most accurately measured data.

Several methods have been proposed to derive optimal vision system configurations. Mittal [5] proposed a formula to assess 3D data errors in terms of the object distance and the cameras' baseline and focal lengths. Hanel *et al.* [6] derived the optimal vision system configuration that makes the visual hull of the detected object more accurate. Cowan and Kovesi [7] generated camera locations such that better image resolutions can be obtained and all the object surface points appear within the cameras' FOVs, unoccluded, and in focus. In these methods, the issues of the variations of pixel-quantization precisions and angular resolutions in images are not considered. In contrast, the method proposed in this study takes these issues into consideration by analyzing the *error propagations* in the 3D data measurement process.

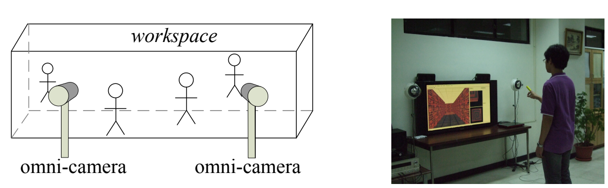

(a) (b)

Fig. 1. Stereo vision system with two omni-cameras for this study. (a) Illustration of the vision system. (b) A user playing a game using the system.

Manuscript received November 4, 2012. This work was supported by the Ministry of Economic Affairs, Taiwan under Project MOEA 98-EC-17-A-02-S1-032 in the Technology Development Program for Academia.

S. E. Shih is with the Institute of Computer Science and Engineering, National Chiao Tung University, Hsinchu, Taiwan 30010. E-mail: peter159.cs98g@nctu.edu.tw.

W. H. Tsai is with the Department of Computer Science, National Chiao Tung University, Hsinchu, Taiwan 30010. He is also with the Department of Information Communication, Asia University, Taichung, Taiwan 41354. E-mail: whtsai@cis.nctu.edu.tw.

Alternatively, the optimal system configuration can be derived by considering the angular error produced by the cameras [8]-[11]. Bishop *et al.* [8] assessed the 3D data measurement error using the Fisher information matrix. Zhao *et al.* [9][10] used the frame theory to prove the existence of only two types of optimal placement of bearing-only sensors. Herath and Pathirana [11] analyzed the sensor-target geometry in terms of the Cramer-Rao inequality and the corresponding Fisher information matrix. However, in these studies the angular information is assumed to include Gaussian noise, and the effects of the variations of pixel-quantization precisions and the angular resolutions yielded by the cameras are ignored, yielding less accurate modeling of 3D data errors. In contrast, the error model proposed in this study takes such effects into consideration via analytic error propagation analysis.

One way to consider the effect of pixel-quantization precision variations is to assess the 3D measurement error by the use of the covariance matrix [12]-[17]. For this, Wenhardt *et al.* [12] determined the locations of mobile cameras to yield the best 3D model reconstruction by assessing the covariance of the resulting 3D data in three ways, namely, using the determinant, eigenvalues, and trace of the covariance matrix, respectively. Hoppe *et al.* [15] used the eigenvalues of the covariance matrix to model the 3D measurement error for precise camera localization and object modeling. Alsadik *et al.* [14] established a camera network for precise reconstruction of a cultural heritage object by the use of the trace of the covariance matrix. Olague and Mohr [16] proposed a multi-cellular genetic algorithm to decide camera locations, which yield minimal 3D measurement errors, by the use of the maximum diagonal element of the covariance matrix. Zhang [13] determined the optimal 2D spatial placement of multiple sensors participating in a robot perception task utilizing the determinant of the covariance matrix. Rivera-Rios, et al. [17] analyzed 3D measurement errors due to feature-point localization errors and found accordingly the optimal camera pose by the mean-square-error criterion using the covariance matrix of the 3D measurement data. In these methods, the precisions of the 3D measurements are all assessed by the use of the covariance matrix. Additionally, a local-affineness assumption is made when deriving the covariance matrix (as stated in [20]). Contrastively, an approach without making this assumption is proposed in this study, which is achieved by detailed analysis of the error propagations in the 3D data computation process. Furthermore, it is shown by experimental results in Section VII.B that the proposed approach yields more precise assessments by a factor of four than the covariance matrix-based methods.

Besides the use of the covariance matrix, some alternative methods have also been proposed to assess the 3D measurement error. Ercan *et al.* [18] studied the problem of the optimal placement of multiple cameras and the selection of the best subset of the cameras for single target localization in a sensor network, with the goal of localizing an object as accurately as possible in the ground plane. The cameras are assumed to be oriented horizontally and far enough from the object. Blostein and Huang [19] analyzed the relationship between the geometry of a stereo camera setup and the accuracy in the obtained 3D measurements. The probability that the position estimates obtained from triangulation are within a specified error tolerance was derived, with the error being modeled as known spatial image plane quantization. The error model is only derived for perspective cameras.

Briefly speaking, the method proposed in this study differs from the existing ones in two aspects: 1) the 3D measurement precision is assessed by error propagation analysis which considers the effect of pixel-quantization precision variations; and (2) the assessed 3D measurement precision is related to the resolutions of the pixels in such a way that a feature point in a higher resolution area is with a lower error in the calculated 3D measurements, and vice versa. As a result, the proposed method can be applied both to perspective cameras and to wide-FOV cameras. Contrarily, the above-mentioned methods make the assumption of *uniform* resolutions across the entire image, which is unreasonable when wide-FOV cameras are used.

Contributions of this study include the following aspects. (1) *Analytic* formulas describing the error propagations in 3D data computation using a binocular omni-camera vision system are derived for assessing the 3D measurement precision. (2) Algorithms for determining the optimal system configuration, including the mirror shape, FOV, and the pose of the two omni-cameras, are derived for use in establishing a more precise stereo vision system. (3) Three optimization algorithms are designed for various environments to meet different applications: one for general cases but slower; another for regular cases but faster, yielding the *optimal* solution by an *iterative* scheme; and the third for regular cases and even faster but finding a near-optimal solution using *analytic* formulas.

In the remainder of this paper, an optimization framework to find the optimal system configuration is proposed in Section II. Some formulas modeling the catadioptric omni-cameras are derived in Section III. A *measure of 3D data accuracy* for use in the optimization process is derived in Section IV. The mentioned three optimization algorithms for finding the optimal system configuration are presented in Sections V and VI. Finally, experimental results and conclusions are given in Sections VII and VIII, respectively.

II. An Optimization Framework

An optimization framework is proposed in this study, as illustrated in Fig. 2, to facilitate the determination of the *optimal system configuration* of a binocular omni-vision system, which includes the intrinsic parameters, locations, and orientations of the two omni-cameras of the system, for the purpose of acquiring the most accurate 3D data. Some observable properties of this frame are: (1) if the two omni-cameras are close to each other, the length of the line segment L connecting the two cameras, namely, *the baseline*, will become small, and the computed 3D data accuracy will so be low; (2) if the baseline is very large, the space points in front of the cameras will become *relatively* close to L, and the resulting accuracy will so be low as well; and (3) since the distortion of an image taken by an omni-camera is significant, the resolution also varies significantly in the taken image so that, if a feature point is located in a higher resolution area, the computed 3D data accuracy will become higher, and vice versa. According to these observed facts, it can be seen that optimal system configurations do exist; therefore, it is meaningful to propose an optimization framework, as conducted in this study, for use in finding the optimal system configuration.

The proposed optimization framework, as depicted in Fig. 2, includes three main steps. First, an area where the 3D data are measured is specified, called the *3D measurement area*; and an area where the cameras can be placed is also specified, called the *camera placement area*. Then, the *optimal* locations, optical axes, and intrinsic parameters of the two omni-cameras are derived according to one of the three proposed system optimization algorithms presented in Sections V.B, V.C, and VI.A, respectively. The three optimization algorithms are based on the use of an *analytic formula* indicating the *degree of accuracy* of the computed 3D data, which is derived according to error propagation analysis as described in Section IV. The found optimal configuration is just the one with the highest degree of 3D data accuracy, which is shown to the user to tell him/her how to place (and/or design) the cameras.

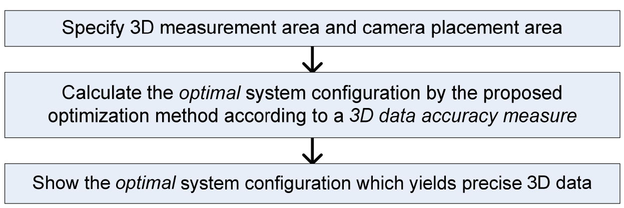

Fig. 2. Proposed optimization framework.

III. Omni-Camera Structure and Formulas

A. Omni-camera Structure

The catadioptric omni-camera is composed of a hyperboloid mirror and a perspective camera looking toward the mirror, as depicted in Fig. 3. A camera coordinate system (CCS) *x*-*y*-*z* and an image coordinate system *u*-*v* are defined in such a way that the *x*- and *y*-axes are parallel to the *u*- and *v*-axes, respectively, and the two focal points of the mirror are at $O(0, 0, 0)$ and $O_c(0, 0, 2c)$. In this way, the mirror shape can be expressed [21] by

$$(z-c)^2/a^2-(x^2+y^2)/b^2=1,\quad c=\sqrt{a^2+b^2},\quad z<c, \tag{1}$$

with its *eccentricity* ε being defined by $c/a > 1$. A *projection equation* describing the relation between the *complementary elevation angle* ϕ of a space point P and image coordinates (u, v) of the projected pixel p can be expressed [22] as

$$\tan\phi=\frac{(\varepsilon^2-1)\sin\tau}{(\varepsilon^2+1)\cos\tau-2\varepsilon}, \tag{2}$$

where $\cos\tau$ and $\sin\tau$, as seen from Fig. 3, can be expressed by

$$\cos\tau=\frac{f}{\sqrt{u^2+v^2+f^2}};\ \sin\tau=\frac{\sqrt{u^2+v^2}}{\sqrt{u^2+v^2+f^2}}. \tag{3}$$

B. Determination of Intrinsic Parameters of Omni-cameras

By assuming the perspective camera in the omni-camera is well-calibrated and distortion-free, the only parameter of the perspective camera is its viewing angle $2\tau_{\max}$. Also, as specified in the projection equation (2), the eccentricity ε describes all the distortion effect produced by the mirror. Therefore, the intrinsic parameters of an omni-camera to be determined are the viewing angle $2\tau_{\max}$ of the perspective camera and the eccentricity ε of the mirror. In the following, we first derive the formula for the eccentricity ε under the assumption that the viewing angle $2\tau_{\max}$ of the perspective camera is fixed. Then, we provide a guideline to determine the angle $2\tau_{\max}$.

Theorem 1. If the viewing angle of the perspective camera is $2\tau_{\max}$ and the viewing angle of the omni-camera is $2\phi_{\max}$, then the eccentricity ε of the hyperboloidal-shaped mirror is

$$\varepsilon=\frac{\sin\phi_{\max}+\sin\tau_{\max}}{\sin(\phi_{\max}-\tau_{\max})}. \tag{4}$$

Proof. According to the projection equation (2), we have

$$(\tan\phi_{\max}-\tan\tau_{\max})\varepsilon^2-2\tan\phi_{\max}\sec\tau_{\max}\varepsilon+(\tan\phi_{\max}+\tan\tau_{\max})=0. \tag{5}$$

Accordingly, two solutions of ε can be obtained to be

$$\varepsilon=\frac{\tan\phi_{\max}\sec\tau_{\max}\pm\tan\tau_{\max}\sec\phi_{\max}}{\tan\phi_{\max}-\tan\tau_{\max}}=\frac{\sin\phi_{\max}\pm\sin\tau_{\max}}{\sin(\phi_{\max}-\tau_{\max})}. \tag{6}$$

The solution ε_1 with the minus sign is proved to be invalid as follows. First, ε_1, as an eccentricity, is larger than one, i.e.,

$$\varepsilon_1=(\sin\phi_{\max}-\sin\tau_{\max})/\sin(\phi_{\max}-\tau_{\max})>1. \tag{7}$$

Next, since the viewing angle $2\phi_{\max}$ of the omni-camera is larger than the viewing angle $2\tau_{\max}$ of the perspective camera, we have $\pi>\phi_{\max}>\tau_{\max}>0$, leading to $\cot(\phi_{\max}/2)<\cot(\tau_{\max}/2)$, which, according to the cotangent half-angle formula [23], results in

$$\cot\left(\frac{\phi_{\max}}{2}\right)=\frac{\sin\phi_{\max}}{1-\cos\phi_{\max}}<\frac{\sin\tau_{\max}}{1-\cos\tau_{\max}}=\cot\left(\frac{\tau_{\max}}{2}\right), \tag{8}$$

or equivalently,

$$\frac{\sin\phi_{\max}-\sin\tau_{\max}}{\sin(\phi_{\max}-\tau_{\max})}=\varepsilon_1<1, \tag{9}$$

which is a contradiction to (7). Therefore, the other solution described by (4) should be taken as the desired result. □

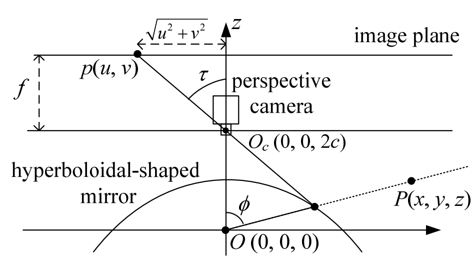

Fig. 3. Catadioptric omni-camera structure and its camera coordinate system.

The effect of choosing different viewing angle $2\tau_{\max}$ of the perspective camera is shown by some images in Fig. 4 obtained from simulations with a checkerboard placed in front of the omni-camera, and the hyperboloidal mirror designed according to Theorem 1 in such a way that the entire checkerboard can be viewed. As seen from Fig. 4, the taken omni-images are not severely influenced by the magnitude of the viewing angle, implying that one may choose freely the viewing angle as long as the camera is distortion-free.

C. Resolution Formula for Omni-cameras

Baker and Nayer [24] proposed a formula to calculate the resolutions at different pixels in an omni-image as follows. Let dA be an infinitesimal area on the image plane near a pixel p, which, as illustrated in Fig. 5, is the projection of an area in the space described by an infinitesimal solid angle $d\nu$ coming from a point P. The resolution of pixel p is formulated as

$$R(\varepsilon, f, \phi) = \frac{dA}{d\nu} = \frac{(\varepsilon^2-1)^2(\varepsilon^2+2\varepsilon\cos\phi+1)}{\left[2\varepsilon+(\varepsilon^2+1)\cos\phi\right]^3} f^2, \tag{10}$$

where ε is the eccentricity of the mirror, f is the focal length of the camera, and ϕ is the complementary elevation angle of P.

IV. Formula for Describing Degree of Accuracy

A criterion function measuring the *degree of accuracy* of the computed 3D data is proposed in this section, for uses in the optimization algorithms proposed in Sections V and VI.

A. 3D Calculation Function and Its Differentials

A right-handed world coordinate system X-Y-Z is defined, as shown in Fig. 6, in such a way that the camera centers O_1 and O_2 are located at $(-D, 0, 0)$ and $(D, 0, 0)$, respectively, and the XY-plane contains the space point P. An assumption that, the two optical axes a_1 and a_2 lie on the XY-plane, is made in the following derivations, and this assumption is analyzed more thoroughly in Section IV.C.

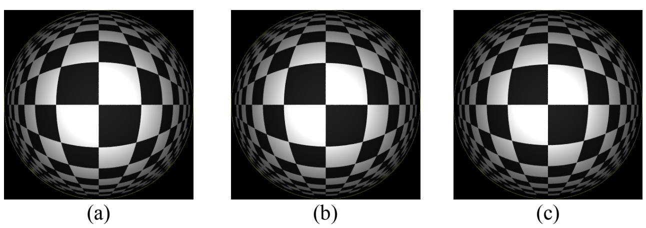

Fig. 4. Simulated omni-images using perspective cameras with different viewing angles: (a) 20°; (b) 40°; and (c) 60°.

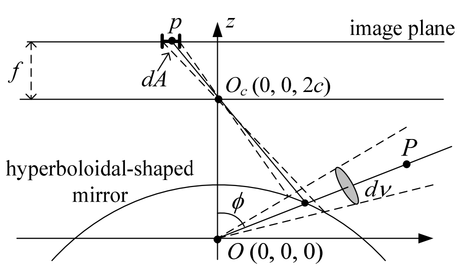

Fig. 5. Illustration for defining the resolution at a pixel.

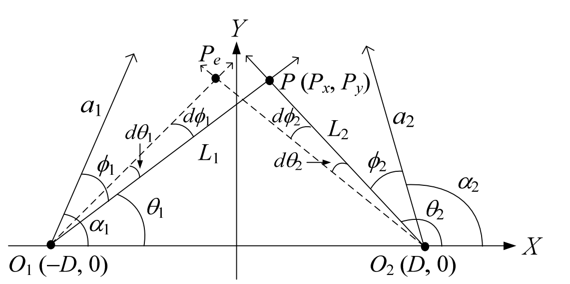

Fig. 6. Top-view illustration of triangulation process and error propagation.

As depicted in Fig. 6, the two axes a_1 and a_2 are defined by the angles α_1 and α_2, respectively. To calculate the 3D data of P, two images are acquired first by the two omni-cameras, and a feature detection process is applied to extract the two pixels p_1 and p_2 corresponding to P in the two omni-images. Then, the complementary elevation angles ϕ_1 and ϕ_2 are derived by (2) using the coordinates of p_1 and p_2, respectively. Finally, the angles θ_1 and θ_2 as depicted in Fig. 6 are computed by:

$$\theta_1 = \alpha_1 - \phi_1, \text{ and } \theta_2 = \alpha_2 - \phi_2. \tag{11}$$

Proposition 1. As depicted in Fig. 6, the position (P_x, P_y) of space point P can be calculated in terms of θ_1 and θ_2 as

$$T(\theta_1, \theta_2) = \left(P_x, P_y\right) = \left(D\frac{\sin(\theta_2+\theta_1)}{\sin(\theta_2-\theta_1)}, 2D\frac{\sin\theta_2\sin\theta_1}{\sin(\theta_2-\theta_1)}\right), \tag{12}$$

and the differentials of P_x and P_y are

$$\begin{bmatrix} dP_x \\ dP_y \end{bmatrix} = \frac{2D}{\sin^2(\theta_2-\theta_1)}\begin{bmatrix} \sin\theta_2\cos\theta_2 d\theta_1 - \sin\theta_1\cos\theta_1 d\theta_2 \\ \sin^2\theta_2 d\theta_1 - \sin^2\theta_1 d\theta_2 \end{bmatrix}. \tag{13}$$

Proof. As depicted in Fig. 6, the position of the feature point P can be calculated by two parametric equations

$$P = O_1 + s_1\cdot(\cos\theta_1, \sin\theta_1);\ \ P = O_2 + s_2\cdot(\cos\theta_2, \sin\theta_2) \tag{14}$$

where P, O_1, and O_2 are regarded as 2D *coordinate vectors*, and s_1 and s_2 are unknown parameters. Eq. (14) is equivalent to:

$$P_x = -D + s_1\cos\theta_1 = D + s_2\cos\theta_2;\ \ P_y = s_1\sin\theta_1 = s_2\sin\theta_2, \tag{15}$$

which may be solved to get s_1 and s_2, leading to the results

$$\begin{aligned} P_x &= D\frac{\sin\theta_2\cos\theta_1+\cos\theta_2\sin\theta_1}{\sin\theta_2\cos\theta_1-\cos\theta_2\sin\theta_1} = D\frac{\sin(\theta_2+\theta_1)}{\sin(\theta_2-\theta_1)}; \\ P_y &= 2D\frac{\sin\theta_1\sin\theta_2}{\sin\theta_2\cos\theta_1-\cos\theta_2\sin\theta_1} = 2D\frac{\sin\theta_2\sin\theta_1}{\sin(\theta_2-\theta_1)}. \end{aligned} \tag{16}$$

And, the differentials of P_x and P_y can be derived accordingly to be those described by (13). □

B. Considering Variations of Pixel-Quantization Precisions and Angular Resolutions

The infinitesimals $d\theta_1$ and $d\theta_2$ are derived by considering the varying pixel-quantization precisions and angular resolutions as follows. As can be seen from Fig. 6, if the feature detection process to extract p_1 and p_2 in the two images is inaccurate so that the angles ϕ_1 and ϕ_2 are with errors $d\phi_1$ and $d\phi_2$, respectively, then an inaccurate triangulation result P_e, as depicted in Fig. 6, will be produced. Assume that the pixel quantization and feature detection process introduces an error within a small area dA, then, as depicted in Fig. 5, the measured angle ϕ will be with an error $d\nu$ related to the *angular resolution* function R. In the sense that $d\nu$ is a 2D solid angle and the angle $d\phi$ is the corresponding 1D angle, and under the assumption that the back-projected cone forming by $d\nu$ is circular, the value of $d\phi$ can be estimated by

$$d\phi = \pm\sqrt{d\nu} = \pm\sqrt{dA/R}, \tag{17}$$

in which the term $d\nu$ is expressed by the resolution formula (10). Also, by taking the differentiations of the equations in (11), one can get a relation between $d\phi$ and $d\theta$ as $d\theta = -d\phi$, which, after being combined with (17), leads to

$$d\theta = \pm\sqrt{dA/R}. \tag{18}$$

Accordingly, the errors $d\theta_1$ and $d\theta_2$ can be derived to be

$$d\theta_1 = \pm\sqrt{\frac{dA}{R(\varepsilon_1, f_1, \phi_1)}}\text{, and } d\theta_2 = \pm\sqrt{\frac{dA}{R(\varepsilon_2, f_2, \phi_2)}}. \quad (19)$$

C. Proposed Error Model and Its Limitations

To assess the 3D measurement error of a feature point P, an error function $E(P)$ is proposed in the following, and the degree of accuracy of the point P is defined as $-E(P)$ in the sequel.

Theorem 2. With reference to Fig. 6, when the triangulation process yields an imprecise point P_e due to small errors $d\theta_1$ and $d\theta_2$, the 3D measurement error $E(P)$, which is the distance between the actual point P and the measured point P_e, is

$$E(P) = \max\left(E_1(P), E_2(P)\right) \quad (20)$$

where

$$E_1(P) = \frac{\sqrt{G_1^{\,2}(P) + 2G_1(P)G_2(P)\cos(\theta_2-\theta_1) + G_2^{\,2}(P)}\sqrt{dA}}{\sin(\theta_2-\theta_1)},$$

$$E_2(P) = \frac{\sqrt{G_1^{\,2}(P) - 2G_1(P)G_2(P)\cos(\theta_2-\theta_1) + G_2^{\,2}(P)}\sqrt{dA}}{\sin(\theta_2-\theta_1)},$$

$$G_1(P) = \frac{\left|\overline{O_1P}\right|}{\sqrt{R(\varepsilon_1, f_1, \phi_1)}}\text{, and } G_2(P) = \frac{\left|\overline{O_2P}\right|}{\sqrt{R(\varepsilon_2, f_2, \phi_2)}}. \quad (21)$$

Proof. The measurement error E, which by definition is the distance between P and P_e, may be computed from (13) to be

$$E(P) = \|dT\| = \sqrt{(dP_x)^2 + (dP_y)^2}$$

$$= \frac{\sqrt{\left(\frac{2D\sin\theta_2 d\theta_1}{\sin(\theta_2-\theta_1)}\right)^2 - 2\cos(\theta_2-\theta_1)\frac{2D\sin\theta_2 d\theta_1}{\sin(\theta_2-\theta_1)}\frac{2D\sin\theta_1 d\theta_2}{\sin(\theta_2-\theta_1)} + \left(\frac{2D\sin\theta_1 d\theta_2}{\sin(\theta_2-\theta_1)}\right)^2}}{\sin(\theta_2-\theta_1)}. \quad (22)$$

From Fig. 6, it can be derived, from the law of sines, that

$$\frac{2D}{\sin(\theta_2-\theta_1)} = \frac{\left|\overline{O_1P}\right|}{\sin\theta_2} = \frac{\left|\overline{O_2P}\right|}{\sin\theta_1}. \quad (23)$$

By combining (22) and (23), we get

$$E(P) = \frac{\sqrt{(\left|\overline{O_1P}\right|d\theta_1)^2 - 2\cos(\theta_2-\theta_1)(\left|\overline{O_1P}\right|d\theta_1)(\left|\overline{O_2P}\right|d\theta_2) + (\left|\overline{O_2P}\right|d\theta_2)^2}}{\sin(\theta_2-\theta_1)}, \quad (24)$$

which, when combined with (19), leads to (20) and (21). □

V. Fast Configuration Optimization for Regular Cases

The optimization framework proposed in Section II can deal with general cases, in which the 3D measurement area and the camera placement area may both be of irregular shapes, and the two used perspective cameras may be different from each other. However, in regular indoor vision systems (called the *regular cases*), the two perspective cameras are of the same type, and the 3D measurement area and the camera placement area can be specified by two rectangular cuboids as illustrated in Fig. 7. In the following, the formal definition of the optimization problem for such regular cases is derived in Section V.A. Then, the derivation of the proposed optimization algorithm for generating the corresponding *optimal* system configuration is proposed in Section V.B. Another *sub-optimal* but *analytic* optimization method is derived in Section V.C, which is shown additionally there to be a good approximation to the optimal solution.

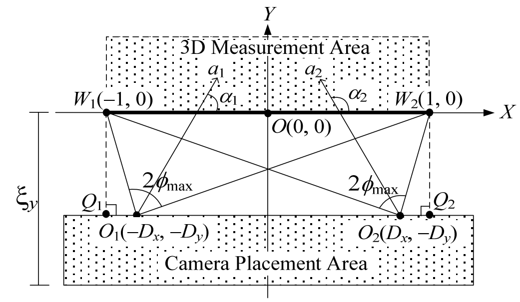

Fig. 7. An illustration of the regular cases.

A. Problem Definition

As described in the optimization framework proposed in Section II, a system configuration includes all the necessary parameters to design a vision system, and an optimization process needs to find the optimal system configuration which yields the best 3D measurement accuracy. A criterion function E_w for the optimization is defined in this study to be the *maximum* measurement error within the 3D measurement area W, i.e.,

$$E_w(W) = \max_{P\in W}\left(E(P)\right), \quad (25)$$

where $E(P)$ is the measurement error of a feature point P as derived by (20) in Theorem 2. By choosing the *maximum* value, *all* the 3D measurements errors are ensured to be lower than the value E_w. Next, as assumed, the two perspective cameras used in the omni-cameras are identical, so their focal lengths f_1 and f_2 are both equal to f, and their viewing angles $2\tau_{max1}$ and $2\tau_{max2}$ are both equal to $2\tau_{max}$. The two omni-cameras are identical in structure and placed symmetrically, so the two optical axes a_1 and a_2 are coplanar so that the two optical axes can be defined by the two angles α_1 and α_2 as shown in Fig. 7. Then, a system configuration can be defined to be the parameter set (D_x, D_y, α_1, α_2, ε_1, ε_2), where (1) the omni-cameras are placed, as seen from the top, at $O_1(-D_x, -D_y)$ and $O_2(D_x, -D_y)$, respectively; (2) the orientations of their optical axes are defined by α_1 and α_2, respectively; and (3) the eccentricities of the mirrors are ε_1 and ε_2, respectively. Hence, the optimization problem is just to find the optimal parameter set (D_x^*, D_y^*, α_1^*, α_2^*, ε_1^*, ε_2^*) derived in the following way:

$$(D_x^*, D_y^*, \alpha_1^*, \alpha_2^*, \varepsilon_1^*, \varepsilon_2^*) = \underset{(D_x, D_y, \alpha_1, \alpha_2, \varepsilon_1, \varepsilon_2)}{\arg\min}\left(E_w(W)\right). \quad (26)$$

Since it is desired that the captured image be fully filled up with the 3D measurement area, the cameras should be oriented to face the 3D measurement area. Accordingly, the optical axes a_1 and a_2 can be figured out to be just the bisectors of the angles spanned by the measurement area as depicted in Fig. 7, that is, the optical axis a_1 of the left omni-camera is the bisector of the viewing angle formed by $\overline{O_1W_1}$ and $\overline{O_1W_2}$, and the optical axis a_2 is the bisector of the viewing angle formed by $\overline{O_2W_1}$ and $\overline{O_2W_2}$. In view of these facts, the angle ϕ_{max} and the optical-axis angles α_1 and α_2 can be calculated in terms of D_x and D_y as follows. First, the fact $\alpha_2 = \pi - \alpha_1$ can be derived from Fig. 7. Then, from the triangle formed by O_1, W_2, and Q_2, we have $D_y = (D_x +$

1)×tan($\alpha_1 - \phi_{max}$). Similarly, from the triangle formed by O_1, W_1, and Q_1, we have $D_y = (D_x - 1) \times \tan(\alpha_1 + \phi_{max})$. Accordingly, the two unknowns α_1 and ϕ_{max} can be solved respectively to be

$$\begin{cases} \alpha_1 = 0.5\left[\tan^{-1}(D_y/D_x - 1) + \tan^{-1}(D_y/D_x + 1)\right]; \\ \phi_{\max} = 0.5\left[\tan^{-1}(D_y/D_x - 1) - \tan^{-1}(D_y/D_x + 1)\right]. \end{cases} \quad (27)$$

Then, based on Theorem 1, the eccentricities ε_1 and ε_2 are

$$\varepsilon_1 = \varepsilon_2 = \varepsilon = (\sin\phi_{\max} + \sin\tau_{\max})/\sin(\phi_{\max} - \tau_{\max}), \quad (28)$$

where $2\tau_{max}$ is the viewing angle of the perspective cameras. To sum up, the optimization problem (26) is now reduced to include two parameters as follows:

$$\left(D_x^*, D_y^*\right) = \underset{(D_x, D_y)}{\arg\min}\left(E_w(W)\right) = \underset{(D_x, D_y)}{\arg\min}\left(\max_{P\in W}\left(E(P)\right)\right). \quad (29)$$

For further simplifications, two claims are given as follows.

Claim 1. The function E_w described by (25) can be rewritten as

$$E_w(W) = \max_{P\in W}\left(E(P)\right) = \max(E(O), E(W_2)), \quad (30)$$

if the two terms $R(\varepsilon, f, \phi_1)$ and $R(\varepsilon, f, \phi_2)$ are equal, where points O and W_2 are located at (0, 0) and (1, 0), respectively.

Proof. At first, by referring to Fig. 8(a), the measurement error of a point P at coordinates (P_x, 0) can be derived using (20) and (21) with

$$\theta_1 = \cos^{-1}\frac{P_x + D_x}{\sqrt{(P_x + D_x)^2 + D_y^2}}, \quad \theta_2 = \cos^{-1}\frac{P_x - D_x}{\sqrt{(P_x - D_x)^2 + D_y^2}},$$

$$G_1(P) = \frac{\sqrt{(P_x + D_x)^2 + D_y^2}}{\sqrt{R(\varepsilon, f, \phi_1)}}, \text{ and } G_2(P) = \frac{\sqrt{(P_x - D_x)^2 + D_y^2}}{\sqrt{R(\varepsilon, f, \phi_2)}}. \quad (31)$$

Next, the function $E(P)$ is proved to be an even function as follows. From Fig. 8(a), the angles ϕ_1 and ϕ_2 can be seen to be

$$\phi_1 = |\alpha_1 - \theta_1|, \text{ and } \phi_2 = |\alpha_2 - \theta_2|. \quad (32)$$

From the resolution formula (10), we can get the equality $R(\varepsilon, f, \phi) = R(\varepsilon, f, -\phi)$ for any angle ϕ. Accordingly, we have

$$R(\varepsilon, f, \phi_1) = R(\varepsilon, f, \alpha_1 - \theta_1);\ R(\varepsilon, f, \phi_2) = R(\varepsilon, f, \alpha_2 - \theta_2). \quad (33)$$

Let P' be the point located at ($-P_x$, 0), and let the related angles θ_1', θ_2', ϕ_1', and ϕ_2' be defined as those shown in Fig. 8(a). Since the triangles $\Delta O_1O_2P'$ and ΔO_1O_2P are similar, we get $\theta_1' = \pi - \theta_2$ and $\theta_2' = \pi - \theta_1$. Combining these facts with (32), we have

$$\begin{aligned} \phi_1' &= |\alpha_1 - \theta_1'| = |(\pi - \alpha_2) - (\pi - \theta_2)| = |-\alpha_2 + \theta_2| = \phi_2; \\ \phi_2' &= |\alpha_2 - \theta_2'| = |(\pi - \alpha_1) - (\pi - \theta_1)| = |-\alpha_1 + \theta_1| = \phi_1. \end{aligned} \quad (34)$$

Thus, the following equality can be derived:

$$G_1(P') = \frac{\sqrt{(-P_x + D_x)^2 + D_y^2}}{\sqrt{R(\varepsilon, f, \phi_1')}} = \frac{\sqrt{(D_x - P_x)^2 + D_y^2}}{\sqrt{R(\varepsilon, f, \phi_2)}} = G_2(P). \quad (35)$$

The function $E_1(P)$ can be proved accordingly to be an even function by

$$\begin{aligned} E_1(P) &= \frac{\sqrt{G_1^2(P) + 2G_1(P)G_2(P)\cos(\theta_2 - \theta_1) + G_2^2(P)}\sqrt{dA}}{\sin(\theta_2 - \theta_1)} \\ &= \frac{\sqrt{G_2^2(P') + 2G_2(P')G_1(P')\cos(\theta_2' - \theta_1') + G_1^2(P')}\sqrt{dA}}{\sin(\theta_2' - \theta_1')} = E_1(P'). \end{aligned} \quad (36)$$

Similarly, we can prove $E_2(P) = E_2(P')$, meaning that $E_2(P)$ is an even function, too.

Finally, we prove in the following the property that if $R(\varepsilon, f, \phi_1)$ and $R(\varepsilon, f, \phi_2)$ are equal, the maximum of $E(P)$ will occurs at $O(0, 0)$ or $W_2(1, 0)$. Firstly, let P_x^* be a value of P_x such that the case $\theta_2 - \theta_1 = 90°$ occurs. When $0 \le P_x \le P_x^*$, we get $90^o \le \theta_2 - \theta_1 \le 180^o$ so that $\cos(\theta_2 - \theta_2) \le 0$, implying that $E_2(P) \le E_1(P)$ according to (21), which leads to the following fact according to (20):

$$E(P) = E_2(P). \quad (37)$$

Furthermore, by applying the law of cosines and the assumption $R(\varepsilon, f, \phi_1) = R(\varepsilon, f, \phi_2)$, $E_2(P)$ can be reduced in the following way:

$$E_2(P) = \frac{\sqrt{|O_1P|^2 - 2|O_1P||O_2P|\cos(\theta_2 - \theta_1) + |O_2P|^2}}{\sin(\theta_2 - \theta_1)} = \frac{|O_1O_2|}{\sin(\theta_2 - \theta_1)}. \quad (38)$$

Accordingly, since the angle $\theta_2 - \theta_1$ decreases from 180^o to 90° when P_x increases from 0 to P_x^*, the maximum of $E(P)$ occurs at $P_x = 0$. For the other case that $P_x^* \le P_x \le 1$, we can get $0^o \le \theta_2 - \theta_1 \le 90^o$ so that $\cos(\theta_2 - \theta_1) \ge 0$, implying that $E_1(P) \le E_2(P)$ according to (21), which leads to the following fact according to (20):

$$E(P) = E_1(P). \quad (39)$$

Furthermore, according to (31), $E_1(P)$ can be expressed as

$$E_1(P) = \frac{\sqrt{|O_1O_2|^2 + 4\overline{PO_1}\cdot\overline{PO_2}}}{\sin(\theta_2 - \theta_1)} = \frac{\sqrt{|O_1O_2|^2 + 4\left(P_x + D_x, D_y\right)\cdot\left(P_x - D_x, D_y\right)}}{\sin(\theta_2 - \theta_1)}. \quad (40)$$

Accordingly, since the angle $\theta_2 - \theta_1$ decreases from 90° to 0^o when P_x increases, the maximum of $E(P)$ occurs at $P_x = 1$. Combine the results of the two cases, we get the conclusion that the maximum occurs at $O(0, 0)$ or $W_2(1, 0)$.

Finally, since both $E_1(P)$ and $E_2(P)$ are even functions, this conclusion may also be proved to hold for the "left-side" range $-1 \le P_x \le 0$. Therefore, the overall conclusion described by (30) may be drawn. □

In the above proof, the assumption $R(\varepsilon, f, \phi_1) = R(\varepsilon, f, \phi_2)$ is made, which is proved later by simulation results to be appropriate with very little affection on the 3D measurement precision of the derived system configuration (see Fig. 12).

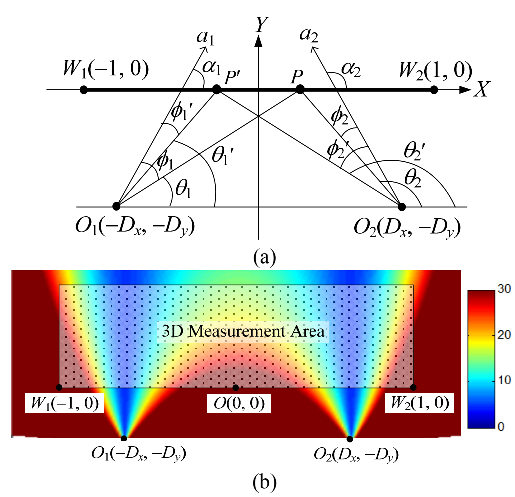

Fig. 8. Analysis of function E_w. (a) Illustrations of related terms. (b) Drawing of distribution of measurement errors E of a configuration.

Claim 2. A larger value of D_y always yields a smaller value of the criterion function E_w.

Proof. The *inscribed angle theorem* says that an angle θ inscribed in a circle is a half of the central angle 2θ that subtends the same arc on the circle [25]. That is, if the viewing angle is $2\phi_{\max}$, the possible positions of the cameras can be figured out to be constrained on the dashed circle shown in Fig. 9(a), and the upper bound of D_y occurs at the bottom of the circle. Also, while recalling that the two cameras are *omni-directional*, we assume their viewing angle $2\phi_{\max}$ to be larger than 120°. So we have

$$\max(D_y) = \cot\phi_{\max} \leq \cot(60°) \approx 0.6. \quad (41)$$

With this upper bound, the function E_w is plotted in Fig. 9(b), which shows that a larger value of D_y yields a smaller value of E_w. □

With Claim 1, Eq. (29) can be re-formulated as

$$(D_x^*, D_y^*) = \underset{(D_x, D_y)}{\arg\min}\left(\max(E(O), E(W_2))\right). \quad (42)$$

Also, recall that the upper bound of D_y is limited by the camera deployment constraint, which we denoted as ξ_y in Fig. 7. With Claim 2, the optimal value D_y^* in (42) can be derived to be $\min(\xi_y, 0.6)$, leaving D_x^* to be the only parameter to be optimized according to the following constraint:

$$D_x^* = \underset{D_x}{\arg\min}\left(\max\left(E_{\text{mid}}(D_x, D_y^*), E_{\text{bound}}(D_x, D_y^*)\right)\right), \quad (43)$$

where E_{bound} and E_{mid} are defined as

$$E_{\text{bound}}(D_x, D_y^*) = E(W_2); \quad E_{\text{mid}}(D_x, D_y^*) = E(O). \quad (44)$$

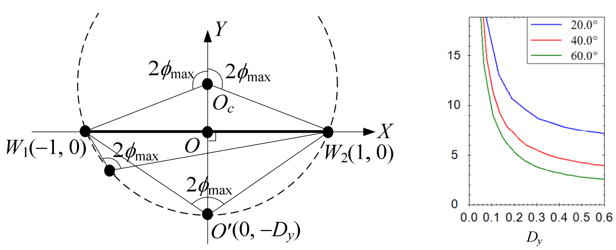

(a) (b)

Fig. 9. Finding the optimal value of D_y (a) An illustration to find the upper bound. (b) A plot of E_w for different values of $2\tau_{\max}$: 20°, 40°, and 60°.

B. Optimization by Numerical Methods

An optimization algorithm to solve D_x^* in (43) by a bisection scheme is proposed in this section. By referring to the plots of E_{mid} and E_{bound} depicted in Fig. 10(a), the optimal solution D_x^* is found at the intersection of the two functions of E_{mid} and E_{bound}. So, if the two functions intersect each other, the intersection point may be defined to be the optimal solution D_x^*; otherwise, the optimal solution D_x^* is defined to be the maximum value which will also be derived later in this section.

In more details, at first we define a new function E_{opt} as

$$E_{\text{opt}}(D_x, D_y^*) = E_{\text{mid}}(D_x, D_y^*) - E_{\text{bound}}(D_x, D_y^*). \quad (45)$$

Then, the optimal solution D_x^* is just the root of E_{opt}, which can be derived by a bisection scheme. Before the scheme is conducted, the initial range of the root must be determined. The lower bound $lower_{Dx}$ of D_x is obviously zero, and the upper bound $upper_{Dx}$ is derived as follows. From Fig. 10(b), we have

$$\left|\overline{O_cO_2}\right| = \left|\overline{O_cW_2}\right| = \csc(\pi - 2\phi_{\max}) = \csc(2\phi_{\max}). \quad (46)$$

And the coordinates of the circle center O_c is

$$O_c = (0, \cot(\pi - 2\phi_{\max})) = (0, -\cot(2\phi_{\max})). \quad (47)$$

According to the Pythagorean Theorem, we have

$$\begin{aligned} D_x^2 &= \left|\overline{O_cO_2}\right|^2 - \left|\overline{O_cO_2'}\right|^2 = \csc^2(2\phi_{\max}) - [D_y^* - \cot(2\phi_{\max})]^2 \\ &= 1 - D_y^*[D_y^* - 2\cot(2\phi_{\max})], \end{aligned} \quad (48)$$

and the first derivative of D_x^2 with respect to $2\phi_{\max}$ is

$$\frac{\partial(D_x^2)}{\partial(2\phi_{\max})} = 2D_y^*(-\csc^2(2\phi_{\max})). \quad (49)$$

Since $D_y^* > 0$, the first derivative of D_x^2 is smaller than zero, meaning that D_x decreases as $2\phi_{\max}$ increases, or equivalently, that the maximum of D_x occurs when $\phi_{\max}$ is minimized. So, the upper bound of D_x can be derived from (48) to be

$$upper_{Dx} = \sqrt{1 - D_y^*[D_y^* - 2\cot(2\phi_{\max})]}. \quad (50)$$

A method to solve the optimization problem is proposed below.

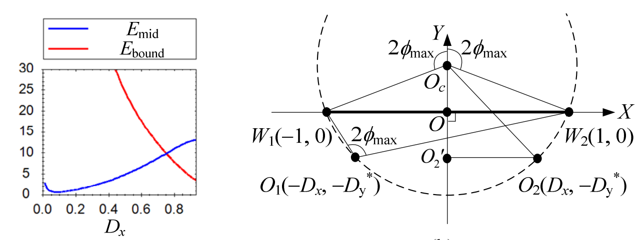

(a) (b)

Fig. 10. Illustrations of finding the optimal solution D_x^* and its upper bound. (a) Plot of E_{mid} and E_{bound} versus D_x when $D_y^* = 0.1$ and $2\tau_{\max} = 60.0°$. (b) Derivation of the upper bound of D_x.

Algorithm 1. *Finding the optimal configuration* (D_x^*, D_y^*).

Input: the viewing angle $2\tau_{\max}$ and the focal length f of the cameras.

Output: the optimal system configuration (D_x^*, D_y^*), meaning that the omni-cameras are placed at $O_1(-D_x^*, D_y^*)$ and $O_2(D_x^*, D_y^*)$, and oriented as shown in Fig. 7.

Steps.

Step 1. Calculate ξ_y according to the deployment size as stated in Section V.A, and set $D_y^* = \min(\xi_y, 0.6)$.

Step 2. Set variable $lower_{Dx} = 0$ and calculate $E_{\text{opt}}(lower_{Dx}, D_y^*)$ as follows and assign the result to the variable *lower*.

- 2.1 Set $D_x = lower_{Dx}$ and calculate $\phi_{\max}$ according to (27).
- 2.2 Calculate the eccentricity ε according to (28).
- 2.3 Calculate E_{mid} and E_{bound} by (44) with $O_1 = (-D_x, D_y^*)$ and $O_2 = (D_x, D_y^*)$, and calculate E_{opt} by (45).

Step 3. Calculate the upper bound $upper_{Dx}$ of D_x^* by (50).

Step 4. Calculate $E_{\text{opt}}(upper_{Dx}, D_y^*)$ in a way similar to Steps 2.1 through 2.3, and assign the result to the variable *upper*.

Step 5. If *lower* and *upper* are with opposite signs, then find the root in a bisecting fashion as follows [26].

5.1. Set variable $new_{Dx} = (lower_{Dx} + upper_{Dx})/2$.

5.2. Calculate $E_{\text{opt}}(new_{Dx}, D_y^*)$ in a way similar to Steps 2.1 through 2.3 and assign the result to the variable *new*.

5.3. If (*new* < *lower*), then set *lower* = *new* and $lower_{Dx} = new_{Dx}$; otherwise, set *upper* = *new* and $upper_{Dx} = new_{Dx}$.

5.4. If $(upper_{Dx} - lower_{Dx}) < \delta$, where δ is a predefined precision threshold, then take $(D_x^*, D_y^*) = (new_{Dx}, \xi_y)$ as the output and exit; otherwise, go to Step 5.1.

Step 6. If *lower* > 0 and *upper* > 0 or if *lower* < 0 and *upper* < 0, then choose D_x^* to be the upper bound $upper_{Dx}$, and take $(D_x^*, D_y^*) = (upper_{Dx}, \xi_y)$ as the output.

C. Derivation of Analytic Formula for Sub-optimal Solution

The method proposed in Algorithm 1 is further simplified to get an analytic formula for deriving a sub-optimal solution. Let v_1 and v_2 be two vectors, and θ be the included angle. We have

$$|v_1 \pm v_2|^2 = (v_1 \pm v_2)\cdot(v_1 \pm v_2) = |v_1|^2 \pm 2|v_1||v_2|\cos\theta + |v_2|^2. \quad (51)$$

By referring to Fig. 11, the formula of the measurement error E_{mid} can be derived, using (44), (20), (21), and (51), to be

$$E_{\text{mid}}(D_x, D_y^*) = \frac{\max\left(\sqrt{\left|\overline{O_1O}\right|^2 \pm 2\left|\overline{O_1O}\right|\left|\overline{O_2O}\right|\cos(\theta_{\text{mid2}}-\theta_{\text{mid1}}) + \left|\overline{O_2O}\right|^2}\right)\sqrt{dA}}{\sin(\theta_{\text{mid2}}-\theta_{\text{mid1}})\sqrt{R(\varepsilon, f, \phi_{\text{mid}})}}$$
$$= \frac{\max\left(\left|\overline{O_1O}+\overline{O_2O}\right|, \left|\overline{O_1O}-\overline{O_2O}\right|\right)\sqrt{dA}}{\sin(\theta_{\text{mid2}}-\theta_{\text{mid1}})\sqrt{R(\varepsilon, f, \phi_{\text{mid}})}} = \frac{\max\left(2D_y^*, 2D_x\right)\sqrt{dA}}{\sin(\theta_{\text{mid2}}-\theta_{\text{mid1}})\sqrt{R(\varepsilon, f, \phi_{\text{mid}})}}. \quad (52)$$

Referring to Fig. 11 and based on the double-angle formula of the sine function, we can get

$$\sin(\theta_{\text{mid2}}-\theta_{\text{mid1}}) = 2\sin\left(\frac{\theta_{\text{mid2}}-\theta_{\text{mid1}}}{2}\right)\cos\left(\frac{\theta_{\text{mid2}}-\theta_{\text{mid1}}}{2}\right) = \frac{2D_y^* D_x}{D_x^2 + (D_y^*)^2}. \quad (53)$$

Thus, the function E_{mid} in (52) can be rewritten as

$$E_{\text{mid}}(D_x, D_y^*) = \frac{\left[D_x^2 + (D_y^*)^2\right]\sqrt{dA}}{\dfrac{2D_y^* D_x\sqrt{R(\varepsilon, f, \phi_{\text{mid}})}}{\max\left(2D_y^*, 2D_x\right)}} = \frac{\left[D_x^2 + (D_y^*)^2\right]\sqrt{dA}}{\min\left(D_x, D_y^*\right)\sqrt{R(\varepsilon, f, \phi_{\text{mid}})}} \quad (54)$$

Similarly, the measurement error E_{bound} of the feature point $W_2(1, 0)$ can be simplified, using (20), (21), (44) and (51), to be

$$E_{\text{bound}}(D_x, D_y^*) = \frac{\max\left(\sqrt{\left|\overline{O_1W_2}\right|^2 \pm 2\left|\overline{O_1W_2}\right|\left|\overline{O_2W_2}\right|\cos(\theta_{\text{max2}}-\theta_{\text{max1}}) + \left|\overline{O_2W_2}\right|^2}\right)\sqrt{dA}}{\sin(\theta_{\text{max2}}-\theta_{\text{max1}})\sqrt{R(\varepsilon, f, \phi_{\text{max}})}}$$
$$= \frac{\max\left(2\sqrt{1+(D_y^*)^2}, 2D_x\right)\sqrt{dA}}{\sin(\theta_{\text{max2}}-\theta_{\text{max1}})\sqrt{R(\varepsilon, f, \phi_{\text{max}})}}. \quad (55)$$

From the geometry shown in Fig. 11, we have

$$\sin(\theta_{\text{max2}}\text{-}\theta_{\text{max1}}) = \sqrt{1-\left(\frac{\overline{O_1W_2}\cdot\overline{O_2W_2}}{\left|\overline{O_1W_2}\right|\left|\overline{O_2W_2}\right|}\right)^2} = \frac{2D_x D_y^*}{\sqrt{\left(D_x^2 + (D_y^*)^2 + 1\right)^2 - 4D_x^2}} \quad (56)$$

Thus, the function E_{bound} in (55) can be rewritten to be

$$E_{\text{bound}}(D_x, D_y^*) = \frac{\sqrt{\left(D_x^2 + (D_y^*)^2 + 1\right)^2 - 4D_x^2}\,\max\left(\sqrt{1+(D_y^*)^2}, D_x\right)\sqrt{dA}}{D_x D_y^*\sqrt{R(\varepsilon, f, \phi_{\text{max}})}}. \quad (57)$$

By combining (54) and (57), the function E_{opt} can be re-formulated as

$$E_{\text{opt}}(D_x, D_y^*) = \frac{\left(D_x^2 + (D_y^*)^2\right)\sqrt{dA}}{\min\left(D_y^*, D_x\right)\sqrt{R(\varepsilon, f, \phi_{\text{mid}})}} - \frac{\max\left(\sqrt{1+(D_y^*)^2}, D_x\right)\sqrt{\left(D_x^2 + (D_y^*)^2 + 1\right)^2 - 4D_x^2}\sqrt{dA}}{D_x D_y^*\sqrt{R(\varepsilon, f, \phi_{\text{max}})}}. \quad (58)$$

To calculate the optimal system configuration, the value D_y^* is firstly derived in the same way as stated in Algorithm 1. Then, the optimal solution D_x^* is just the root of the function E_{opt} described by (58). However, the root does not have an analytic formula since the involved terms ϕ_{mid}, ϕ_{max} and ε are all with complicated formulas with respect to D_x. In order to derive an analytic solution for the root, we first propose a skillful approximation method to produce a new function E_{opt}' to approximate the original one E_{opt}, and then derive an analytic formula to compute a sub-optimal solution D_x'. This sub-optimal solution D_x' is a good approximation to the optimal one D_x^* as will be shown later in this section.

To simplify the function E_{opt} described by (58), we assume further

$$R(\varepsilon, f, \phi_{\text{mid}}) \approx R(\varepsilon, f, \phi_{\text{max}}), \quad (59)$$

which is a special case of the assumption $R(\varepsilon, f, \phi_1) = R(\varepsilon, f, \phi_2)$ made before in the proof of Claim 1. This new assumption can be proved as well later by simulation results to be proper with very little affection on the 3D measurement precision of the derived system configuration (see Fig. 12). Consequently, Equation (58) may now be simplified to be

$$E_{\text{opt}}'(D_x,\ D_y^*) = \left(\frac{\sqrt{dA}}{\sqrt{R(\varepsilon, f, \phi_{\text{max}})}}\right)\times$$
$$\left(\frac{D_x^2 + (D_y^*)^2}{\min\left(D_y^*, D_x\right)} - \frac{\max\left(\sqrt{1+(D_y^*)^2}, D_x\right)\sqrt{[D_x^2 + (D_y^*)^2 + 1]^2 - 4D_x^2}}{D_x D_y^*}\right). \quad (60)$$

Thus, the root D_x' of the equation $E_{\text{opt}}'(D_x, D_y^*) = 0$ satisfies

$$\frac{(D_x')^2 + (D_y^*)^2}{\min\left(D_y^*, D_x'\right)} = \max\left(\sqrt{1+(D_y^*)^2}, D_x'\right)\frac{\sqrt{[(D_x')^2 + (D_y^*)^2 + 1]^2 - 4(D_x')^2}}{D_x' D_y^*}. \quad (61)$$

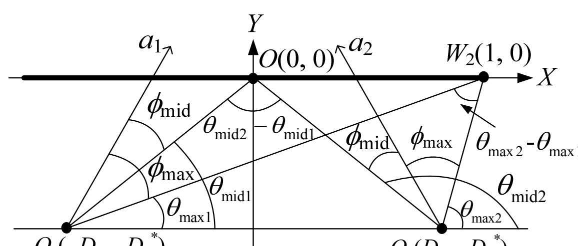

Fig. 11. Related parameters involved in E_{mid} and E_{bound}.

Theorem 3. The solution of D_x' in (61) is

$$D_x' = \sqrt{\frac{-4(D_y^*)^4 - (C-2)(D_y^*)^2 - C^2 + C + 5}{3C}}, \quad (62)$$

where

$$C = \sqrt[3]{0.5Q - 8(D_y^*)^6 - 48(D_y^*)^4 - 46.5(D_y^*)^2 - 5.5};$$
$$Q = \sqrt{27\left(1+(D_y^*)^2\right)\left(128(D_y^*)^8 + 352(D_y^*)^6 + 288(D_y^*)^4 + 75(D_y^*)^2 + 23\right)}. \quad (63)$$

Proof. To deal with the involved min/max function in (61), four cases are discussed separately, which are: (1) $D_x' < D_y^*$ and $D_x' \le (1+(D_y^*)^2)^{0.5}$; (2) $D_x' < D_y^*$ and $D_x' > (1+(D_y^*)^2)^{0.5}$; (3) $D_x' \ge D_y^*$ and $D_x' \le (1+(D_y^*)^2)^{0.5}$; and (4) $D_x' \ge D_y^*$ and $D_x' > (1+(D_y^*)^2)^{0.5}$. It is proved next that only Case (3) is valid.

For Case (1), we have the assumptions $D_x' < D_y^*$ and $D_x' \le (1+(D_y^*)^2)^{0.5}$, so that (61) can be reduced to be

$$\frac{(D_x')^2+(D_y^*)^2}{D_x'} = \sqrt{1+(D_y^*)^2}\,\frac{\sqrt{[(D_x')^2+(D_y^*)^2+1]^2-4(D_x')^2}}{D_x'D_y^*}, \quad (64)$$

or equivalently, to be

$$D_y^*[(D_x')^2+(D_y^*)^2] = \sqrt{1+(D_y^*)^2}\,\sqrt{[(D_x')^2+(D_y^*)^2+1]^2-4(D_x')^2}\,. \quad (65)$$

Defining $A = (D_x')^2$ and $B = (D_y^*)^2$, Eq. (65) can be expressed as

$$A^2 - 2A + (3B^2 + 3B + 1) = 0. \quad (66)$$

Since the discriminant of (66) is $4 - 4(3B^2 + 3B + 1) < 0$, the solution of A does not exist, or equivalently, D_x' does not exist. As a result, the assumptions made for Case (1) are invalid.

The assumptions made for Case (2) are $D_x' < D_y^*$ and $D_x' > (1+(D_y^*)^2)^{0.5}$. Since these two inequalities are contradictory to each other, Case (2) is also out of consideration.

For Case (4), the two assumptions are $D_x' \ge D_y^*$ and $D_x' > (1+(D_y^*)^2)^{0.5}$. Thus, Equation (61) can be rewritten to be

$$(D_x')^2+(D_y^*)^2 = \sqrt{[(D_x')^2+(D_y^*)^2+1]^2-4(D_x')^2}\,. \quad (67)$$

Defining $A = (D_x')^2$, $B = (D_y^*)^2$ and taking the squares of both sides of the above equation, we have $(A + B)^2 = (A + B + 1)^2 - 4A$, or equivalently, $2A = 2B + 1$. However, from the second assumption $D_x' > (1+(D_y^*)^2)^{0.5}$, we get $A > B + 1$, which is a contradiction to the equation $2A = 2B + 1$ derived previously. Therefore, the assumptions made for Case (4) are also invalid.

As a result, Case (3) is the only valid one, for which the two assumptions are $D_x' \ge D_y^*$ and $D_x' \le (1+(D_y^*)^2)^{0.5}$. Accordingly, Equation (61) can be rewritten to be

$$\frac{(D_x')^2+(D_y^*)^2}{D_y^*} = \sqrt{1+(D_y^*)^2}\,\frac{\sqrt{[(D_x')^2+(D_y^*)^2+1]^2-4(D_x')^2}}{D_x'D_y^*}, \quad (68)$$

or equivalently, to be

$$aA^3 + bA^2 + cA + d = 0 \quad (69)$$

where $A = (D_x')^2$, $B = (D_y^*)^2$, $a = 1$, $b = B - 1$, $c = 2 - B^2$, and $d = -(B + 1)^3$. To find the solution of A for the cubic function (69), we first calculate its discriminant Δ, according to [27], as

$$\begin{aligned}\Delta &= 18abcd - 4b^3d + b^2c^2 - 4ac^3 - 27a^2d^2 \\ &= -(B + 1)(128B^4 + 352B^3 + 288B^2 + 75B + 23), \end{aligned} \quad (70)$$

which is smaller than zero because $B = (D_y^*)^2 > 0$. Thus, we get to know that the cubic polynomial equation has only one real root which can be described by (62) according to [27]. □

The above-described process of generating the sub-optimal configuration (D_x', D_y^*) is summarized as an algorithm below.

Algorithm 2. *Finding a sub-optimal configuration* (D_x', D_y^*) *by analytic formulas.*

Input: the viewing angle $2\tau_{\max}$ and the focal length f of the cameras.

Output: the sub-optimal configuration (D_x', D_y^*), meaning that the omni-cameras are placed at $O_1(-D_x', D_y^*)$ and $O_2(D_x', D_y^*)$, and oriented as shown in Fig. 7.

Steps.

Step 1. Calculate ξ_y according to the deployment size as stated in Section V.A, and set $D_y^* = \min(\xi_y, 0.6)$.

Step 2. Calculate the upper bound $upper_{Dx}$ of D_x^* by (50).

Step 3. Calculate D_x' by (62) derived in Theorem 3.

Step 4. Set $D_x' = \min(D_x', upper_{Dx})$.

Step 5. Output the optimal system configuration (D_x', D_y^*).

The sub-optimal configuration (D_x', D_y^*) is shown to be *a good approximation* to the optimal one (D_x^*, D_y^*) as follows. Recalling that the goal of the optimization is to minimize the measurement error E_w defined by (43), we use the function E_w as a criterion to analyze the precision of the approximate one. In Fig. 12, we plot the curves of the measurement error values of the optimal and sub-optimal configurations for all the possible values of D_y, from which we see that the measurement errors are very close to each other, meaning that the sub-optimal configuration also yields precise 3D measurement results as the optimal configuration does. Also, we use a *difference ratio* defined by

$$(E_w' - E_w^*) / E_w^* \quad (71)$$

to determine the *goodness* of the performance of the sub-optimal configuration, where E_w^* and E_w' denote the measurement errors using the optimal and sub-optimal configurations, respectively. As shown in the figure, the difference ratio is smaller than 0.4%, showing that the sub-optimal solution is indeed a good approximation.

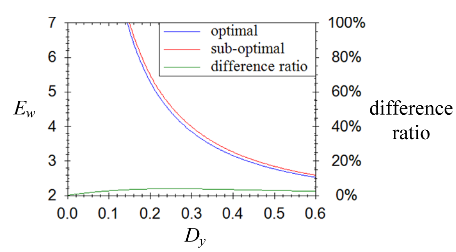

Fig. 12. Comparison of optimal configuration (D_x^*, D_y^*) and sub-optimal configuration (D_x', D_y^*) with viewing angle $2\tau_{\max} = 60°$.

VI. Optimization for General Cases

A. Idea of System Optimization for General Cases

To design a system configuration for the general case, the *3D measurement area* and the *camera placement area* are specified first. To make the descriptions of the possibly irregular shapes of the two areas easy, each area is described by multiple *sampled points*, called the *3D measurement locations* and *camera placement locations*, respectively. For example, a cuboid can be described by 10000 evenly-distributed points. The occlusion problem can be handled by just eliminating the camera locations where the 3D measurement locations will be partially occluded if the camera was placed there [29].

After the 3D measurement locations and the camera placement locations are both identified, the optimal system configuration can be found out as follows (see Fig. 13 for a flowchart). At First, two locations are chosen from the camera placement locations to be the positions of the left and right cameras, respectively. Then, the cameras are oriented to face the 3D measurement area as described next in Section VI.B to determine the extrinsic parameters of the omni-cameras. Also, their intrinsic parameters, including the mirror-shape parameter and the viewing angle of the perspective camera, are determined by the method proposed in Section III.

To decide which configuration yields the most precise 3D measurements, a measure indicating the degree of accuracy of the computed 3D data defined as $\min(-E(M_i))$ is calculated, where $-E(M_i)$ is the degree of accuracy of a 3D measurement location M_i as derived in Theorem 2. It is noted that, by choosing the *minimum* value, *all* the 3D measurement locations are ensured to be at least with this degree of accuracy. Then, to find the optimal system configuration, the previously-described steps are executed repeatedly for all possible camera locations as shown by the loop in Fig. 13, and the configuration with the highest degree of accuracy is picked out finally as the desired result.

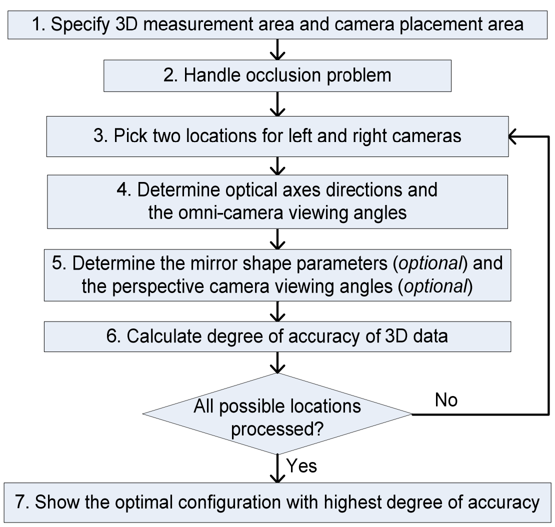

Fig. 13. Proposed optimization process to deal with general cases.

B. *Determination of Camera's Optical Axes and View Angles*

After the positions of the two omni-cameras are decided, it is necessary to determine the optical axis and the viewing angle of each omni-camera. To solve this problem, the camera should face the 3D measurement locations, and this in turn determines the orientations of the camera. Specifically, let M_i denote the points in the 3D measurement locations, and O the chosen location of each omni-camera (i.e., the camera center). Then, the problem may be solved, as depicted in Fig. 14, by three steps: (1) find the smallest viewing cone containing all the 3D measurement locations M_i and with O as its apex; (2) set the optical axis as the viewing cone axis; and (3) take the viewing angle $2\phi_{\max}$ of the omni-camera to be the aperture of the cone.

C. *Speed-Up Techniques*

To speed up the optimization method described in Fig. 13, three techniques are proposed as follows.

(1) *Longest baseline first*. When picking up the locations of the cameras in Step 3, the ones with large baselines (i.e., the distance between the cameras) are picked up first.

(2) *Farthest 3D point first*. When calculating the 3D data accuracy in Step 6, the 3D points which are farther from the two cameras are calculated first.

(3) *Early stopping*. If the computed 3D data accuracy is larger than that of the so-far best configuration, then the current configuration cannot be a better one, and so the algorithm continues to perform Step 3 for the next configuration.

These techniques were implemented and tested by experiments, and the results show that they reduced the running time from 56.6 seconds down to 22.3, indicating a speedup of about 2.5 times.

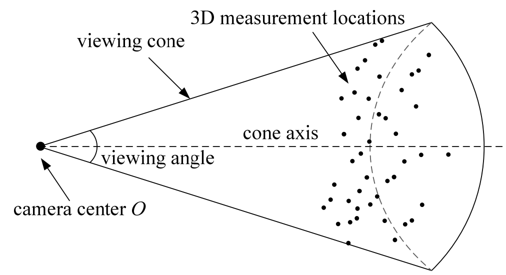

Fig. 14. An illustration of finding the optical axis and the viewing angle.

D. *Choosing Optimization Methods for Different Applications*

Three optimization methods have been proposed in Sections V.B, V.C, and VI, for the regular-optimal, regular-suboptimal, and general cases, respectively. These methods have their own advantages and disadvantages as described in the following.

(1) If the 3D measurement area and the camera placement area are both approximately of rectangular shapes, the first and second methods can be used; otherwise, the third one.

(2) If the optimization process can be done in an off-line fashion, the third method is suitable; otherwise, the first two methods should be used.

(3) If it requires a fast computation time, or the system has a low computation capability, the first two methods are suitable; and among the two, the second is the faster one but a little bit less accurate.

Some possible applications are stated next to demonstrate the uses of the three optimization methods. When designing a vision system for home entertainment, exhibitions, wide-area video surveillance, etc., since the camera positions can be derived in advance and the environment may be irregular-shaped and possibly with occlusions, the third optimization method should be used. However, if the cameras can be oriented automatically by computer, the first optimization method may be used in an online fashion to achieve better 3D measurement accuracies. On the other hand, if the cameras are mounted, for example, on unmanned vehicles to collect wide-area 3D information in realtime, the second optimization method should be used because fast computations according to analytic formulas can be conducted, and the saved computation power can be used for navigation, learning, event recognition, etc.

VII. Experimental Results

In this section, the experimental results of a case study of finding the optimal system configuration in a simulated indoor environment are described first in Section VII.A. And the proposed method is then compared with four existing methods by experimental results for a real laboratory environment in Section VII.B.

A. A Case of Constructing an Indoor Stereo Vision System

A room with size 10m×2.5m×3m, as depicted in Fig. 15(a), was considered, and the 3D data of a user's body moving within the 3D measurement area were required to be calculated accurately. Also, the omni-cameras need be designed and placed in the camera placement area. In the following, the optimal system configuration for this simulation case study is derived first using the proposed method. Then, comparisons of the 3D measurement accuracies yielded by the optimal system configuration and some non-optimal ones are presented.

1) Finding Optimal System Configuration

To find the optimal system configuration, a coordinate system is defined first as depicted in Fig. 15(a) with the floor being taken to be the plane $Z = 0$, and the viewing angles $2\tau_{\max}$ of the perspective cameras chosen to be 60°. Next, about 100 evenly distributed points were generated in the 3D measurement area, and about 1000 similarly distributed points were generated in the camera placement area. Then, the optimization process proposed in Section VI.A (depicted in Fig. 13) was applied to such a *general* case of environment. And the generated configuration with the minimum 3D measurement error was chosen finally to be the desired optimal system configuration S_1^*, which, as illustrated in Fig. 15(a), includes: (1) the locations O_1 and O_2 of the two cameras at ($\mp$3.92m, –0.5m, 2.5m), respectively; (2) the optical axes a_1 and a_2 oriented in accordance with the vectors (±0.093, 0.996, 0.0), respectively; and (3) the eccentricities ε_1 and ε_2 of the mirrors both being 1.8967. The images taken by the two cameras were simulated by a ray tracing program POV-Ray, with two examples shown in Figs. 15(b) and 15(c).

Alternatively, the above problem of vision system design can be seen as a 2D one, in which only the XY-plane is considered, and the two cameras are installed at the middle height of 2.5m (recalling that the room is with a height of 5m). As depicted in Fig. 16(a), let W be the boundary line $\overline{W_1W_2}$ of the 3D measurement area which is nearer to the camera placement area, and let C be the boundary line of the camera placement area which is farther to the workspace. The 2D coordinate system is defined in such a way that the coordinates of W_1 and W_2 are (–1, 0) and (1, 0), respectively. In this sense, a unit in the coordinate system represents 5m in real space, so that the distance ξ_y between the line segments W and C, as depicted in Fig. 16, can be derived to be 0.1. Then, with the use of ξ_y, the two proposed optimization schemes described by Algorithms 1 and 2 in Section V were performed to such a *regular* case of environment to derive the optimal two camera locations.

The *optimal* camera locations derived by Algorithm 1 are ($\mp$0.753, –0.1) in the 2D coordinate system, which then were mapped back to the world coordinate system. Subsequently, the methods proposed in Sections VI.B and III.B were applied to find the optical axes directions and eccentricities, yielding the optimal system configuration S_2^*, which includes: (1) the locations O_1 and O_2 of the two cameras at ($\mp$3.766m, –0.5m, 2.5m), respectively; (2) the optical axes a_1 and a_2 oriented in accordance with the vectors (±0.163, 0.987, 0.0), respectively; and (3) the eccentricities ε_1 and ε_2 of the mirrors both being 2.0067. In a similar way, the *sub-optimal* system configuration S_3^* were derived by applying Algorithm 2 and the methods proposed in Sections VI.B and III.B, which includes: (1) the locations O_1 and O_2 of the two cameras at ($\mp$3.822m, –0.5m, 2.5m); (2) the optical axes a_1 and a_2 oriented in accordance with the vectors (±0.172, 0.985, 0.0), respectively; and (3) the eccentricities ε_1 and ε_2 both being 2.0194. It can be seen that the data of the two configurations S_2^* and S_3^* are quite close as expected.

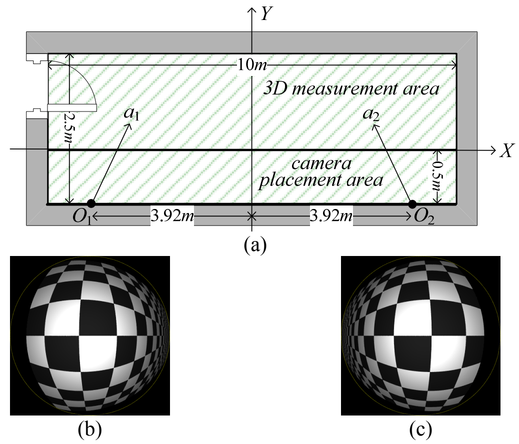

Fig. 15. Optimal system configuration for the general case derived by the optimization process proposed in Section VI. (a) An illustration of the optimal system configuration. (b)(c) Simulated images taken by the two cameras, with 3D measurement area drawn as a checkerboard cube.

2) Comparison of 3D Measurement Accuracies

To compare the 3D measurement accuracies yielded by the three different optimal system configurations S_1^*, S_2^*, and S_3^* derived in the previous section, three additional system configurations S_1, S_2 and S_3 were chosen arbitrarily, in which the two cameras are located at (±2.5m, –0.5m, 2.5m) in configuration S_1, at (±1.67m, –0.5m, 2.5m) in S_2, and at (±3.33m, –0.5m, 2.5m) in S_3. Their optical axes' directions were calculated as proposed in Section VI.B, and the eccentricities of the two mirrors were calculated by the scheme described in Section III.B.

Similar to the experiments described in 1) of this section, about 10,000 points were uniformly generated in the 3D measurement area. Each of the 10,000 point was firstly back-projected onto the two omni-images with coordinates (u_1, v_1) and (u_2, v_2). Then, Gaussian noise with zero means and standard deviations 1.0 (pixel) were applied to the four coordinate values, and the estimated location of the 3D point was calculated accordingly by mid-point triangulation [28]. The distance between the ground-truth 3D point and the estimated 3D point was then computed as the 3D measurement error. The minimum, maximum, and standard deviation of the 3D measurement errors resulting from the 10,000 points are listed in Table I. Also, the function E proposed in Section IV was used to estimate the maximum 3D measurement errors, whose minimum, maximum, and standard deviation values are also listed in Table I for comparison. Note that, since the values calculated by the use of E are unitless, they were scaled in such a way that the standard deviations are the same as the one derived with Gaussian noise added.

Recall that a good system configuration is one with a small *maximum* 3D measurement error (listed in the 3rd column with bold fonts in Table I). Accordingly, we can see that the three optimal system configurations S_1^*, S_2^*, and S_3^* are better. Also, recall that the function E is proposed to estimate these maximum values for use as a criterion to find the optimal system configuration. The effectiveness of E in this aspect can be seen from the similarity of the maximum values **max** listed in the 3rd columns of Table I to those listed in the 6th column.

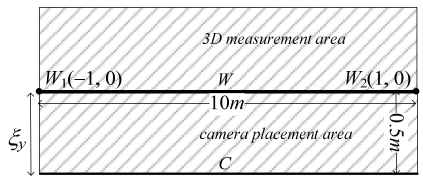

Fig. 16. The corresponding 2D problem of the case study.

TABLE I. 3D MEASUREMENT ERRORS

System config.	3D measurement errors			Estimated 3D measurement error (by proposed method)		
	min [cm]	**max [cm]**	std. [cm]	min[a]	**max[a]**	std.[a]
S_1^*	0.395	**12.287**	1.965	4.127	**12.499**	1.965
S_2^*	0.393	**12.673**	2.000	3.860	**11.799**	2.000
S_3^*	0.385	**12.379**	1.985	4.004	**11.579**	1.985
S_1	0.342	**22.773**	3.235	1.655	**17.159**	3.235
S_2	0.362	**15.196**	2.223	2.704	**12.950**	2.223
S_3	0.314	**36.685**	5.326	1.078	**27.236**	5.326

[a]The values are scaled such that the standard deviations are the same as the ones derived with Gaussian noise added.

B. Comparisons with Existing Methods

1) Introduction to Existing Methods

The proposed method to assess the 3D measurement error is based on analytic error propagation analysis, as described in Section IV. Another approach found popular in the literature is to use the covariance matrix to assess the 3D measurement error [12]-[17] as surveyed in Section I. Four different methods of this approach were implemented by programs in this study. They are briefly introduced first here and then compared with the proposed method by experimental results in this section.

When using the covariance matrix to assess the 3D measurement error yielded by a binocular vision system, let P be a feature point in the space, (u_1, v_1) be the coordinates of the pixel P' corresponding to P in the left-camera image, and (u_2, v_2) be those of P' in the right-camera image. By mid-point triangulation [28], if the 3D location of P is calculated by a function $f(u_1, v_1, u_2, v_2)$, then, according to [30], the covariance matrix Σ_P of the measured 3D location data of P can be assessed by

$$\Sigma_P = \left(\partial f / \partial p\right) \Sigma_p \left(\partial f / \partial p\right)^T, \tag{72}$$

where p is the vector (u_1, v_1, u_2, v_2), Σ_p is the covariance matrix of p, and T denotes the operation of matrix transpose. The covariance matrix Σ_p can be estimated in complicated ways [12]-[16] or by constant values [13][17]. For simplicity, the matrix was estimated by an identity matrix in our implementations, and the first-order derivatives of f were obtained by a finite difference approach [31] with the difference taken to be 10^{-10}. After the covariance matrix Σ_P is derived, the four implemented methods use the following data of Σ_P to assess the 3D measurement error: (1) the determinant [12][13], (2) the trace [12][14], (3) the maximum eigenvalue [12][15], and (4) the maximum diagonal element [16]. These four different methods are named *DET*, *TR*, *MAXEIG*, and *MAXDIAG*, respectively, subsequently.

2) Comparisons of Proposed Error Model with Others

A simulation environment for comparisons of the proposed error model with others is constructed as follows. The 3D measurement area is defined to be rectangular-shaped with two corners located at $(-1, 0, -1)$ and $(1, 0, 1)$, including about 100,000 equidistant points for use as the 3D measurement locations. The two omni-cameras were placed at $(\pm 0.7, -0.1, 0)$, and the viewing angles of the used perspective cameras are 60° and the resolution of acquired images is 600×600. In each simulation, two omni-images were taken firstly, and the projections of each 3D measurement location L_i were extracted as two pixels l_i and r_i in the left and right omni-images, respectively. To simulate the imprecision introduced by the feature detection process, noise values within the range from -1.0 to 1.0 were introduced into the coordinates of the extracted pixels l_i and r_i. The mid-point triangulation process [28] was then conducted to compute the 3D position L_i' of each landmark point located at L_i using the coordinates of image pixels l_i and r_i. Since the coordinate values were interfered with noise, the calculated 3D position L_i' is slightly different from the ground truth L_i. With the recall that the measurement error is defined as the distance between the actual point and the measured one (see Section IV), the measurement error yielded by the simulation was computed accordingly to be $\|L_i - L_i'\|$.

The above simulation was conducted several times, and an average measurement error was calculated for each landmark point as plotted in Fig. 17(a). These average measurement errors are considered as ground-truth values, and were compared with the measurement errors calculated by the proposed error model and those proposed by the four implemented existing methods shown in Figs. 17(b) through 17(f), respectively. The peak signal-to-noise ratio (PSNR) values and the running times of the five methods are listed in Table II, from which one can see that the proposed error model yields the highest PSNR, and the *TR* method is the best of the four existing methods in this aspect but worse than the proposed model by a factor of $10^{(2.367 - 1.760)} = 10^{0.607} \approx 4.04$, and the running time of the proposed method is smaller than that of the *TR* method by a factor of $273.97/8.56 \approx 32.01$.

3) Comparisons of the Optimization Algorithms

In this section, we describe the derivation of the optimal configuration of a vision system for a real laboratory environment. In the environment, a user was allowed to move freely in a specified 3D measurement area, and the two omni-cameras were placed within a specified camera placement area. The optimal positions and orientations of the two omni-cameras were computed for this environment by the proposed method and the four existing methods mentioned previously.

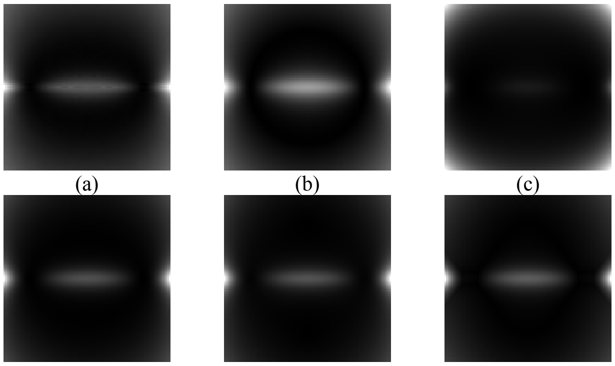
(a) (b) (c) (d) (e) (f)

Fig. 17. Images for 3D measurement errors (with darker colors indicating smaller errors) calculated by (a) simulations, (b) proposed method, (c) method *DET* [12][13], (d) method *TR* [12][14], (e) method *MAXEIG* [12][15], and (f) method *MAXDIAG* [16].

TABLE II
PSNR VALUES AND RUNNING TIMES IN THE SIMULATION

Method	PSNR	Running Time
Proposed error model	23.67dB	8.56 milliseconds
Method *DET* [12][13]	12.07dB	273.22 milliseconds
Method *TR* [12][14]	17.60dB	273.97 milliseconds
Method *MAXEIG* [12][15]	15.32dB	344.03 milliseconds
Method *MAXDIAG* [16]	15.24dB	277.24 milliseconds

Specifically, as shown in Fig. 18(a), the floor of the environment is the *XY*-plane, the 3D measurement area is the cuboid with two diagonal points being (5.0, 2.0, 2.0) and (−5.0, 0.0, 0.0), and the camera placement area is the rectangle on the plane $Z = 0$ with two diagonal points being (5.0, 0.0, 1.0) and (−5.0, −0.5, 1.0). The goal of the optimization algorithm is to find the optimal positions O_1 and O_2 of the two omni-cameras, and their optical axes directions a_1 and a_2, such that the 3D measurements of an object located in the 3D measurement area are as accurate as possible. The two cameras are hyperboloidal catadioptric ones with eccentricity ε being 1.6571, the viewing angle of the perspective camera is $2\tau_{max} = 38°$, and the omni-image size is 600×600.

The optimization process was conducted firstly for a general case as stated in Section VI-A. At first, some points, for use as 3D measurement locations, were sampled within the 3D measurement area with a fixed interval 10*cm*, and some points, for use as the camera placement locations, were sampled within the camera placement area with a fixed interval 1*cm*. Then, for each possible positions O_1 and O_2 of the cameras, the directions of the optical axes were derived as stated in VI.B, and the 3D measurement error were assessed by the error model proposed in Section IV. Finally, the poses of the two omni-cameras which yield the minimum 3D measurement error were taken to be the parameters of the best system configuration. The result of this process says that two cameras should be placed at (±3.78, −0.5, 1.0), respectively, and the optical axes be oriented in accordance with the vectors ($\mp$ 0.14, 0.99, 0.0), respectively.

To test the 3D measurement accuracy using such a system configuration, a checker board were placed on the planes with Y = 0.0, 1.0, and 2.0 in the 3D measurement area, as shown in Figs. 19(a) and 19(b). The image pixels corresponding to all the *cross points* were manually picked out from the captured omni-images, and the obtained coordinates of these pixels were disturbed with additive noise within the range [–5, 5] to simulate errors introduced by the feature detection process. Then, by mid-point triangulation [28], the 3D data of the cross points were derived, called the *measured data*. Finally, the 3D measurement errors were taken to be the distances between the measured data and the ground-truth data, the latter being measured manually in advance. The 3D measurement errors of the cross points on the calibration board at plane $Y = 0.0$ are drawn in Fig. 19(c), whose shape, as can be found, is consistent with that of Fig. 8(b) or Fig. 17(b), though depicted in different ways. Also, these results of the proposed method are listed in Table III for comparison with those obtained similarly of the aforementioned four existing methods. As can be seen from the table, the proposed method yields the minimum measurement errors, and runs faster than the others for about 20 times.

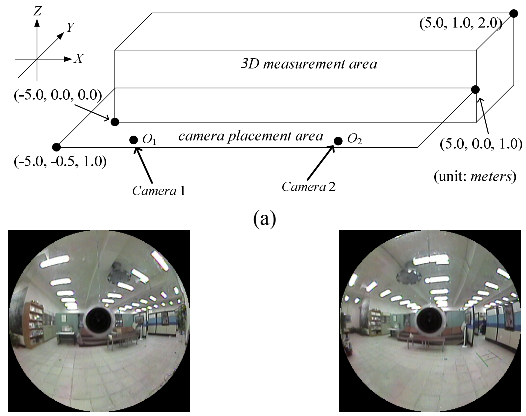

(a)

(b) (c)

Fig. 18. Environment where experiments were conducted. (a) An illustration. (b)(c) Two omni-images captured in the environment.

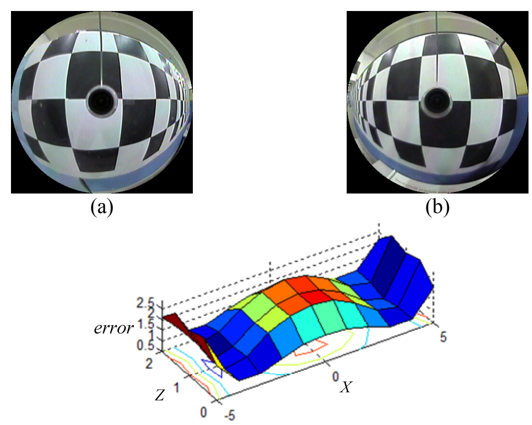

(a) (b)

(c)

Fig. 19. Testing the 3D measurement accuracy of the derived best system configuration. (a)(b) A checkerboard is placed at $Y = 0$ to test the accuracy. (c) The 3D measurement errors of the points on the board.

TABLE III
THE OPTIMIZATION RESULTS OF THE METHODS

Method	Two Cameras' Positions (unit: *meter*)	Maximum 3D Measurement Error (unit: *cm*)	Run Time (unit: *sec*)
Proposed method	(±3.78, –0.5, 1.0)	26.290	11.413
Method *DET* [12][13]	(±4.02, –0.5, 1.0)	29.185	216.927
Method *TR* [12][14]	(±3.95, –0.5, 1.0)	28.007	217.241
Method *MAXEIG* [12][15]	(±3.94, –0.5, 1.0)	27.843	254.599
Method *MAXDIAG* [16]	(±3.88, –0.5, 1.0)	26.877	220.423

VIII. Conclusion

The issue of designing the optimal configuration of a stereo vision system with two catadioptric omni-cameras to compute 3D data with minimum errors is investigated in this study. The solution includes the poses and the mirror-shape parameters of the omni-cameras. An analytic formula is derived to model the 3D measurement error, which takes into consideration the error propagation in the data computation process. Two fast and elegant optimization algorithms have been designed accordingly for "regular" environments with rectangular cuboid-shaped 3D measurement and camera placement areas. One of them, based on a bisection scheme, is optimal but relatively slower, which may be used for off-line applications. And the other, using analytic formulas to calculate approximate solutions, is faster for realtime applications with the computed precision being sub-optimal but close to that of the former. An algorithm for dealing with general environments with irregular-shaped 3D measurement and camera placement areas has also been developed for general uses. Experimental results show the feasibility of the proposed method.

In real applications, a manufacturer may produce omni-cameras according to the derived optimal mirror shape. Then, a consumer may bring them back and deploy them in the optimal or nearly-optimal pose using the proposed algorithms. As a result, a stereo vision system which yield precise 3D measurement results can be set up. Future studies may be directed to generalizing the proposed optimization method to a stereo vision system with more than two omni-cameras.

References

[1] P. Eisert and B. Girod, "Automatic reconstruction on stationary 3-D objects from multiple uncalibrated camera views," *IEEE Trans. on Circuits and Systems for Video Technology*, vol. 10, no. 2, pp. 261-277, 2000.

[2] G. Wang and Q. M. J. Wu, "Perspective 3-D Euclidean reconstruction with varying camera parameters," *IEEE Trans. on Circuits and Systems for Video Technology,* vol. 19, no. 12, pp. 1793-1803, 2009.

[3] P. F. Sturm and B. Triggs, "A factorization based algorithm for multi-image projective structure and motion," *Proc. 4th Euro. Conf. Computer Vision*, vol. 2, Cambridge, U. K., pp. 709-720, 1996.

[4] J. Starck, A. Maki, S. Nobuhara, A. Hilton and T. Matsuyama, "The multiple-camera 3-D production studio," *IEEE Trans. Circuits and Systems for Video Technology*, vol. 19, no. 6, pp. 856-869, June, 2009.

[5] A. Mittal, "Generalized Multi-Sensor Planning," *Proc. European Conference on Computer Vision*, pp. 522-535, 2006.

[6] M. Hanel, S. Kuhn, D. Henrich, J. Pannek, and L. Grune, "Optimal Camera Placement to Measure Distances Conservativly Regarding Static and Dynamic Obstacles," *Int. Journal of Sensor Networks*, vol. 12, no. 1, pp. 25-36, 2012.

[7] C. K. Cowan and P. D. Kovesi, "Automatic sensor placement from vision task requirements," *IEEE Trans. Pattern Analysis and Machine Intelligence*, vol. 10, no. 3, pp. 407–416, May 1998.

[8] A. N. Bishop, B. Fidan, B. D. O. Anderson, K. Dogancay, and P. N. Pathirana, "Optimality Analysis of Sensor-Target Localization Geometries," *Journal of Automatica*, vol. 46, no. 3, pp. 479-492, 2010.

[9] S. Zhao, B. M. Chen, and T. H. Lee, "Optimal Placement of Bearing-only Sensors for Target Localization," *Proc. American Control Conf.* pp. 5108-5113, 2012.

[10] S. Zhao, B. M. Chen, and T. H. Lee, "Optimal Sensor Placement for Target Localization and Tracking in 2D and 3D," *eprint arXiv:1210.7397*, 2012.

[11] S. C. K. Herath and P. N. Pathirana, "Optimal Sensor Separation for AoA Based Localization Via Linear Sensor Array," *Proc. International Conference on Intelligent Sensors, Sensor Networks and Information*, pp. 187-192, 2010.

[12] S. Wenhardt, B. Deutsch, E. Angelopoulou, and H. Niemann, "Active Visual Object Reconstruction using D-, E-, and T-Optimal Next Best Views," *Proc. IEEE Conf. on Computer Vision and Pattern Recognition*, pp. 1-7, 2007.

[13] H. Zhang, "Two-dimensional optimal sensor placement," *IEEE Trans. Systems, Man, and Cybernetics*, vol. 25, no. 5, pp. 781–792, 1995.

[14] B. Alsadik, M. Gerke, and G. Vosselman, "Automated Camera Network Design for 3D Modeling of Cultural Heritage Objects," *Journal of Cultural Heritage*, 2013.

[15] C. Hoppe, A. Wendel, S. Zollmann, and S. Kluckner, "Photogrammetric Camera Network Design for Micro Aerial Vehicles," *Proc. 17th Computer Vision Winter Workshop*, Feb. 2012.

[16] G. Olague, and R. Mohr, "Optimal camera placement for accurate reconstruction," *Pattern Recognition*, vol. 35, no. 4, pp. 927–944, 2002.

[17] A. H. Rivera, F. L. Shih, and M. Marefat, "Stereo camera pose determination with error reduction and tolerance satisfaction for dimensional measurements," in *Proc. IEEE Int. Conf. Robotics and Automation*, pp. 423–428, April 2005.

[18] A. O. Ercan, D. B. Yang, A. E. Gamal, and L. J. Guibas, "Optimal placement and selection of camera network nodes for target localization," in *Proc. IEEE Int. Conf. Distributed Computing in Sensor Systems*, pp. 389–404, 2006.

[19] S. D. Blostein and T. S. Huang, "Error analysis in stereo determination of 3-D point positions," *IEEE Trans. Pattern Analysis and Machine Intelligence*, vol. 9, no. 6, pp. 752−765, Nov. 1987.

[20] R. Hartley and A. Zisserman. *Multiple View Geometry in Computer Vision.* Cambridge University Press, 2000.

[21] C. Geyer and K. Daniilidis, "Catadioptric projective geometry," *Int. J. of Computer Vision*, vol. 45, no. 3, pp. 223−243, 2001.

[22] C. J. Wu and W. H. Tsai, "An omni-vision based localization method for automatic helicopter landing assistance on standard helipads," *Int. Conf. Computer and Automation Engineering*, pp. 327−332, 2010.

[23] M. Abramowitz and I. A. Stegun, *Handbook of Mathematical Functions With Formulas, Graphs, and mathematical Tables*. pp. 72.

[24] S. Baker and S. Nayar, "A theory of single-viewpoint catadioptric image formation," *Int. J. of Computer Vision*, vol. 35, no. 2, pp. 175−196, 1999.

[25] D. Pedoe, *Circles: A Mathematical View (Spectrum)*, 2nd ed. The Mathematical Association of America, 1997.

[26] T. H. Cormen, C. E. Leiserson, and R. L. Rivest, *Introduction to Algorithms*. New York: McGraw-Hill, 1990.

[27] R. S. Irving, *Integers, Polynomials, and Rings.* New York: Springer, 2004.

[28] R. Hartley and P. Sturm, "Triangulation," *Proc. ARPA Image Understanding Workshop*, pp. 957–966, 1994.

[29] M. Berg, M. Kreveld, M. Overmars, and O. Schwarzkopf, *Computational Geometry: Algorithms and Applications.* New York: Springer, 1997.

[30] O. Faugeras, *Three-Dimensional Computer Vision: A Geometric Viewpoint*, MIT Press, Cambridge, MA, 1996.

[31] J. E. Dennis and R. B. Schnabel, *Numerical Methods for Unconstrained Optimization and Nonlinear Equations*, Prentice Hall, 1983.

Shen-En Shih received the B.S. degree in computer science from National Chiao Tung University, Taiwan, in 2009, and is currently pursuing the Ph.D. degree at the College of Computer Science, National Chiao Tung University. He has been a research assistant at the Computer Vision Laboratory in the Department of Computer Science at National Chiao Tung University from August 2009. His current research interests include computer vision, image processing, human-machine interfacing, and stereo vision.

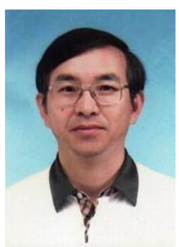

Wen-Hsiang Tsai (S'78-M'79-SM'91) received the B.S. degree from National Taiwan University, Taiwan, in 1973, the M.S. degree from Brown University, USA in 1977, and the Ph.D. degree from Purdue University, USA in 1979, all in electrical engineering. Since 1979, he has been with National Chiao Tung University (NCTU), Taiwan, where he is now a Chair Professor of Computer Science. At NCTU, he has served as a department head, the dean of general affairs and academic affairs, and a vice president. From 1999 to 2000, he was the Chair of the Chinese Image Processing and Pattern Recognition Society of Taiwan, and from 2004 to 2008, the Chair of the Computer Society of the IEEE Taipei Section in Taiwan. From 2004 to 2007, he was the President of Asia University, Taiwan.

Dr. Tsai has been an editor or the editor-in-chief of several international journals and is currently an associate editor of *IEEE Transactions on Information Forensics and Security*. He has published 156 journal papers and 245 conference papers and received more than 40 awards, including the Annual Paper Award from the Pattern Recognition Society of the USA; the Academic Award of the Ministry of Education, Taiwan; the Outstanding Research Award of the National Science Council, Taiwan; and the ISI Citation Classic Award from Thomson Scientific. His research interests include computer vision, information security, video surveillance, and autonomous vehicle applications. He is a Life Member of the Chinese Pattern Recognition and Image Processing Society, Taiwan, and a Senior Member of the IEEE.